5-14-2019

The Impact of Shadows on Partitioning of Radiometric Temperature to Canopy and Soil Temperature Based on the Contextual Two-Source Energy Balance Model (TSEB-2T)

Mahyar Aboutalebi
Utah State University, mahyar.aboutalebi@gmail.com

Alfonso F. Torres-Rua
Utah State University, alfonso.torres@usu.edu

Mac McKee
Utah State University, mac.mckee@usu.edu

Hector Nieto
Complutum Tecnologas de la Informacin Geogrfica

William Kustas
U.S. Department of Agriculture

Calvin Coopmans
Utah State University, cal.coopmans@usu.edu

Recommended Citation

Mahyar Aboutalebi, Alfonso F. Torres-Rua, Mac McKee, Hector Nieto, William Kustas, and Calvin Coopmans "The impact of shadows on partitioning of radiometric temperature to canopy and soil temperature based on the contextual two-source energy balance model (TSEB-2T)", Proc. SPIE 11008, Autonomous Air and Ground Sensing Systems for Agricultural Optimization and Phenotyping IV, 1100804 (14 May 2019); http://dx.doi.org/10.1117/12.2519685

PROCEEDINGS OF SPIE

SPIEDigitalLibrary.org/conference-proceedings-of-spie

The impact of shadows on partitioning of radiometric temperature to canopy and soil temperature based on the contextual two-source energy balance model (TSEB-2T)

Mahyar Aboutalebi, Alfonso F. Torres-Rua, Mac McKee, Hector Nieto, William Kustas, et al.

Mahyar Aboutalebi, Alfonso F. Torres-Rua, Mac McKee, Hector Nieto, William Kustas, Calvin Coopmans, "The impact of shadows on partitioning of radiometric temperature to canopy and soil temperature based on the contextual two-source energy balance model (TSEB-2T)," Proc. SPIE 11008, Autonomous Air and Ground Sensing Systems for Agricultural Optimization and Phenotyping IV, 1100804 (14 May 2019); doi: 10.1117/12.2519685

SPIE.

Event: SPIE Defense + Commercial Sensing, 2019, Baltimore, Maryland, United States

Best Paper Award

The impact of shadows on partitioning of radiometric temperature to canopy and soil temperature based on the contextual two-source energy balance model (TSEB-2T)

Mahyar Aboutalebi*[a], Alfonso F. Torres-Rua[a], Mac McKee[a], Hector Nieto[b], William Kustas[c], and Calvin Coopmans[d]

[a]Utah Water Research Laboratory, Department of Civil and Environmental Engineering, Utah State University, 8200 Old Main Hill, Logan, UT, USA.
[b]COMPLUTIG, Complutum Tecnologas de la Informacin Geogrfica.S.L, Madrid, Spain.
[c]U. S. Department of Agriculture, Agricultural Research Service, Hydrology and Remote Sensing Laboratory,Beltsville, MD, USA.
[d]Electrical Engineering Department, Utah State University, 8200 Old Main Hill, Logan, UT, USA.

ABSTRACT

Tests of the most recent version of the two-source energy balance model have demonstrated that canopy and soil temperatures can be retrieved from high-resolution thermal imagery captured by an unmanned aerial vehicle (UAV). This work has assumed a linear relationship between vegetation indices (VIs) and radiometric temperature in a square grid (i.e., 3.6 m x 3.6 m) that is coarser than the resolution of the imagery acquired by the UAV. In this method, with visible, near infrared (VNIR), and thermal bands available at the same high-resolution, a linear fit can be obtained over the pixels located in a grid, where the x-axis is a vegetation index (VI) and the y-axis is radiometric temperature. Next, with an accurate VI threshold that separates soil and vegetation pixels from one another, the corresponding soil and vegetation temperatures can be extracted from the linear equation. Although this method is simpler than other approaches, such as TSEB with Priestly-Taylor (TSEB-PT), it could be sensitive to VIs and the parameters that affect VIs, such as shadows. Recent studies have revealed that, on average, the values of VIs, such as normalized difference vegetation index (NDVI) and leaf area index (LAI), that are located in sunlit areas are greater than those in shaded areas. This means that involving or compensating for shadows will affect the linear relationship parameters (slope and bias) between radiometric temperature and VI, as well as thresholds that separate soil and vegetation pixels. This study evaluates the impact of shadows on the retrieval of canopy and soil temperature data from four UAV images before and after applying shadow compensation techniques. The retrieved temperatures, using the TSEB-2T approach, both before and after shadow correction, are compared to the average temperature values for both soil and canopy in each grid. The imagery was acquired by the Utah State University AggieAir UAV system over a commercial vineyard located in California as part of the USDA Agricultural Research Service Grape Remote sensing Atmospheric Profile and Evapotranspiration Experiment (GRAPEX) Program during 2014 to 2016. The results of this study show when it is necessary to employ shadow compensation methods to retrieve vegetation and soil temperature directly.

Keywords: TSEB, LAI, Evapotranspiration (ET), GRAPEX, AggieAir, UAS, UAV

1. INTRODUCTION

In general, shadows are formed by an elevated object blocking a light source. Specifically, shadows are classified into three categories: urban shadow, topographic shadow, and cloud shadow. The impact of urban shadows is highlighted in the higher resolution imagery and urban regions. This type of shadow is generated by a building or tree totally or partially occluding light. Topographic shadow is usually the main problem in mid-resolution

Further author information: (Send correspondence to Mahyar Aboutalebi)
Mahyar Aboutalebi: E-mail: Mahyar.Aboutalebi@gmail.com

Autonomous Air and Ground Sensing Systems for Agricultural Optimization and Phenotyping IV
edited by J. Alex Thomasson, Mac McKee, Robert J. Moorhead, Proc. of SPIE Vol. 11008,
1100804 · © 2019 SPIE · CCC code: 0277-786X/19/$18 · doi: 10.1117/12.2519685

and mountainous areas. Cloud shadows can appear in high- to low-resolution imagery (Shahtahmasebi et al. 2013[1]).

High-resolution imagery from UAVs provides detailed information that offers a great opportunity for precision water management in agricultural fields. However, the increased resolution accentuates the impact of shadows that obscure feature information in the affected area, (Dare, 2005[2]), reduce spectral response, and enormously degrade the visual quality of the images. While shadows can be a useful source of information for extracting geometrical information about an object (Aboutalebi et al. 2019[3]), they can affect the performance of optical sensors and hinder correct object classification, object recognition, and change detection (Singh et al. 2012[4]) at high spatial resolutions where elevation varies dramatically across short distances (Tolt et. al, 2011[5]).

Due to the impact of shadows on the accuracy of image processing analysis, many effective shadow detection and compensation methods have been proposed and tested. These algorithms can be classified into three categories: threshold-based approaches, 3D modeling, and machine learning. In general, threshold-based algorithms suffer from misclassification of dark but non-shaded pixels into shadows. Currently, 3D modeling is popular, but its application is limited to cases for which digital surface and digital terrain models are available. In shadow detection processes that use machine learning algorithms, objects with inherently low reflectance such as water bodies are mistaken for shaded areas (Chen et al. 2007[6] and Garousi-Nejad et al. 2019[7]). Aboutalebi et al. (2018a[8]) evaluated the performance of several threshold-based and 3D modeling algorithms in detecting shaded and sunlit pixels in a vineyard. They concluded that the accuracy of threshold-based algorithms is higher than 3D modeling, although the performance of both threshold-based and 3D modeling are comparable with a manual shadow extraction method. Tolt et. al (2011[5]) separated shadow and non-shadow regions using a 3D model algorithm and then used those regions as training records for a machine learning model called support vector machine (SVM). Although shadow compensation is more challenging than shadow detection, three popular algorithms produce a shadow-free image: the linear correlation method (Sarabandi et al, 2004[9]), gamma correction (Massalabi et al, 2004[10]) and histogram matching (Tsai, 2004[11]).

In addition, researchers have used the developed shadow algorithms to evaluate the behavior of spectral response for different objects when they are located in sunlit and shaded areas. Yamazaki et al. (2009[12]) investigated the spectral characteristics of a white plate when located in sunlit areas and light and dark shadows. They found that the ratio of the radiance in the shadow and in the sunlit area increases as the sunlight gets weaker. The results also indicated that the shadow effect is a function of time, casting conditions, and the sunlit wavelength. Aboutalebi et al. (2018b[13]) evaluated the behavior of several VIs in shaded and sunlit areas over a vineyards using AggieAir UAv imagery. They found that the VI differences in shaded and sunlit pixels are significant and the mean values of the VIs in sunlit pixels are higher than those in shaded areas.

Although shadow detection, shadow compensation, and the behavior of spectral response and vegetation indices (VIs) have been assessed, the impact of de-shadowing algorithms on evapotranspiration (ET) models working with aerial imagery is untouched. Limited research has been conducted that shows the importance of shadows on energy fluxes. However, the influence of shadows on the outcome of ET models is more apparent when an ET remote sensing model is developed based on the empirical relationship between VIs and ET input. Aboutalebi et al. (2018a[8]) considered two scenarios to evaluate the impact of shadows on the energy balance component from the Two-Source Energy Balance (TSEB) model. The scenarios involved and masked shaded pixels in evapotranspiration calculations. The results illustrated the significant effect of shadows on energy balance components, particularly on soil heat flux. However, the results were not compared with flux tower records, and the performance of the TSEB model after applying a de-shadowing algorithm remained questionable.

This study used a new version of TSEB called TSEB-2T, which was presented by Nieto et al. (2018[14]). This version partitions the radiometric temperature into canopy and soil temperature, and assumes a linear relationship between VIs and radiometric temperature at a higher resolution. The study compares the TSEB-2T results in four scenarios: original imagery, shadow masking (shadow removal), shadow compensation using a linear correlation correction (LCC), and shadow compensation using gamma correction (GC). In each scenario, the TSEB-2T model's inputs are the same except for Tc and Ts. Since NDVIs are affected in these four scenarios, four different Ts and Tc datasets are extracted based on contextual linear relationships. TSEB-2T is executed using these four different datasets and the results are compared to the flux tower measurements (observed records.)

2. MATERIALS AND METHODS

2.1 Area of Study and UAV Sensor Description

For the current study, three high-resolution images (finer than 20 cm) were captured by a small UAV in August 2014 and in June and July 2015 over a Pinot Noir vineyard located near Lodi, California (38.29 N 121.12 W), in Sacramento County as part of the GRAPEX project. These UAV flights were synchronized with Landsat satellite overpass dates and times. The UAV was operated by the AggieAir UAV Research Group at the Utah Water Research Laboratory at Utah State University. In addition to the high-resolution imagery, 270 LAI measurements were acquired in the field on those dates using the Plant Canopy Analyzer (PCA, LAI2200C, LI-COR, Lincoln, NE, USA) as the indirect in-situ LAI measurements.

The study area employs a drip-irrigated system in which irrigation lines run along the base of the trellis at 30 cm agl with two emitters between each vine. The training system in the vineyard was "U" shaped trellises with canes trained upwards. The vine trellises were 3.35 m apart, and the heights to the first and second cordons were about 1.45 and 1.9 m, respectively (Kustas et al. 2018[15]).

Figure 1 shows the study area with examples of images captured by UAV and NASA phenocam. Camera and optical filter information, fieldwork dates, vineyard phenological stages, and imagery resolution are summarized in Tables 1 and 2.

Figure 1. Example of an aerial image of the study area captured by the AggieAir UAV (top), and NASA phenocam photographs for the same site (bottom)

Table 1. Dates, times, cameras, and optical filters used to capture images with the UAV

Date	UAV Flight Time (PDT)		UAV elevation	Bands		Cameras and Optical Filters		Spectral Response
	Launch Time	Landing Time	(agl) meters	RGB	NIR	Radiometric Response	MegaPixels	
August 9, 2014	11:30 AM	11:50 AM	450	Cannon S95	Cannon S95 modified (Manufacturer NIR block filter removed)	8-bit	10	RGB: typical CMOS NIR: extended CMOS NIR Kodak Wratten 750 nm LongPass filter
June 2, 2015	11:21 AM	12:06 PM	450	Lumenera Lt65R Color	Lumenera Lt65R Monochrome	14-bit	9	RGB: typical CMOS NIR: Schneider 820 nm LongPass filter
July 11, 2015	11:26 AM	12:00 PM	450	Lumenera Lt65R Color	Lumenera Lt65R Monochrome	14-bit	12	RGB: typical CMOS NIR: Schneider 820 nm LongPass filter

Table 2. Dates, optical, DSM and thermal resolution, point cloud density and phenological stages of the vineyard when the images were captured by the UAV

Date	Optical and DSM resolution	Thermal resolution	Point cloud density (point/mˆ2)	Phenological stage
20140809	15 cm	60 cm	37	near harvest
20150602	10 cm	60 cm	118	near veraison
20150711	10 cm	60 cm	108	veraison to harvest

According to Tables 1 and 2, the UAV imagery covers all three major phenological vineyard stages: near veraison, veraison to harvest, and near harvest. The thermal resolution for all four flights was 60 cm and the VNIR were 10 cm, except for the August flight. Cameras ranged from consumer-grade Canon S95 cameras to industrial type Lumenera monochrome cameras fitted with longpass filters.

Imagery acquisition was followed by a two-step image processing phase that included (1) radiometric calibration and (2) image mosaicking and orthorectification. For radiometric calibration, the raw images (digital number) are converted into a measure of reflectance according to the ratio of reference images capturing from pre- and post-flight Labsphere Lambertian panel readings. This study employs a method developed by Neale and Crowther, 1994[16]; and Crowther, 1992[17]). For image mosaicking and orthorectification, all images were merged into one mosaic and rectified using the Agisoft Photoscan software[18], with control point coordinates measured by a Real-Time Kinematic (RTK) GPS instrument. The output of this step is an orthorectified reflectance mosaic (Elarab et al. 2015[19]). For thermal imagery processing, only step 2 is applied. The resulting thermal mosaic was brightness temperature in degrees Celsius. Moreover, a vicarious calibration for atmospheric correction of microbolometer temperature sensors proposed by Torres-Rua[20] was used to refine the thermal images.

2.2 Methodology

The methods used in the study are described in Fig 2.

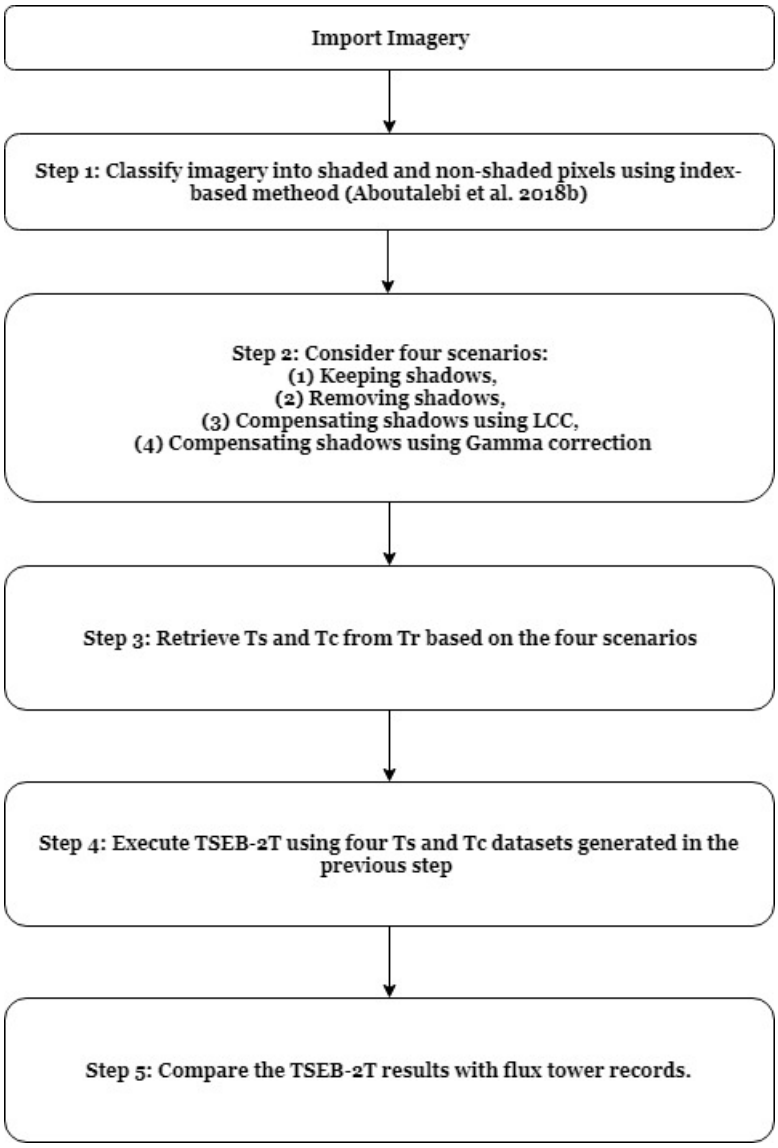

Figure 2. A flowchart illustrating the process of the study

As outlined in Fig 2, the first step involves classifying the three sets of the AggieAir UAV imagery captured over a vineyard in 2014 to 2015 into two categories: shaded regions and non-shaded regions. The shadow detection method is based on the study conducted by Aboutalebi et al. (2018a[8]) on these images, in which they evaluated the performance of four different shadow detection methods (index-based, physical-based, supervised, and unsupervised classification) on high-resolution imagery captured by AggieAir. They found that the index-based method detected shaded pixels more accurately than the other three classification methods. In step 2, four different scenarios are defined to assess the impact of shadows and shadow compensation techniques on the separation of Tr into Ts and Tc. These scenarios are as follows: (1) keeping shaded pixels (original imagery), (2) shadow removal, (3) shadow compensation using Gamma Correction (GC), and (4) shadow compensation using the linear correlation correction (LCC). Aboutalebi et al. (2018b[13]) evaluated the performance of two shadow compensation techniques on high-resolution imagery to recover the shaded regions and the impact on VIs. Results indicated that there is a significant difference between soil/vegetation indices in sunlit and shaded pixels and that this difference can be diminished by applying shadow restoration techniques. In the second scenario, shadow removal, the shaded pixels are removed from the imagery and Ts and Tc are retrieved solely

based on sunlit pixels. In step 3, a Ts and Tc retrieval technique using Tr and NDVI presented by Nieto et al. (2018[14]) is applied on four scenarios. Nieto et al. (2018[14]) assumed a linear relationship between Tr and VIs at high-resolution analysis, and knowing the pure values of NDVI for canopy and soil, Ts and Tc can be extracted from Tr. Thus, in this step, four different sets of Ts and Tc are generated based on the scenarios. In the last step, the TSEB-2T model is executed for each of the scenarios and is compared with flux tower records. This comparison will highlight the importance of shadow restoration techniques on the performance of remote sensing ET models such as TSEB-2T.

2.2.1 Shadow Detection: Index-based

In this study, the index-based shadow detection method tested by Aboutalebi et al. (2018a[8]) is used to classify the images into shaded and non-shaded layers. This method converts the multi-spectral imagery into a gray-scale image and extracts the dark pixels using thresholds defined by histogram analysis.

2.2.2 Shadow Compensation 1: Linear Correlation Correction

Linear correlation correction (LCC) is a popular shadow correction method that increases the values of shaded pixels using a linear equation. This equation is a function of standard deviation and the mean value of shaded and sunlit pixels (Eq. (1), Sarabandi 2004[9]).

$$DN_{recovered} = \frac{\sigma_{non-shadow}}{\sigma_{shadow}}(DN_{shadow} - \mu_{shadow}) + \mu_{non-shadow}\,, \tag{1}$$

in which $DN_{recovered}$ = digital number for recovered shaded pixels, DN_{shadow} = digital number for shaded pixels, $\sigma_{non-shadow}$= standard deviation of sunlit pixels, σ_{shadow} = standard deviation of shaded pixels, μ_{shadow} = mean of shaded pixels, $\mu_{non-shadow}$ = mean of sunlit pixels.

2.2.3 Shadow Compensation 2: Gamma Correction

Gamma correction is the second method used in the study to recover the shaded pixels. Similar to LCC, Gamma correction increases the values of dark pixels but uses a nonlinear function. This function is defined in Eq. (2) and is a function of shaded values and one parameter, Sarabandi 2004[9].

$$DN_{recovered} = DN_{shadow}^{\frac{1}{\lambda}}\,, \tag{2}$$

where λ is a parameter that can be determined using Eq. 3 (Aboutalebi et al. 2018[13]).

$$\lambda = \frac{\mu_{Ln(DN_{shadow})}}{\mu_{Ln(DN_{nonshadow})}}\,, \tag{3}$$

in which $\mu_{Ln(DN_{shadow})}$ = mean of the logarithmic value of the digital number for shaded pixels, and $\mu_{Ln(DN_{nonshadow})}$= mean of the logarithmic value of the digital number for sunlit pixels.

2.2.4 TSEB-2T

TSEB-2T is a TSEB model that was developed for direct retrieval of Ts and Tc from Tr by searching pure vegetation and soil pixels in a contextual spatial domain (Nieto et al. 2018[14]). The contextual domain is a 3.6 x 3.6 m grid mapping NDVIs versus Tr (Fig 3). Next, a linear function is fitted on the NDVI-Tr pairs. Pure vegetation and soil pixel values are defined using histogram analysis for the entire field. These threshold values are substituted into the fitted linear equation and two temperatures are retrieved. The lowest and highest temperatures are assigned for Tc and Ts, respectively. In addition to Ts and Tc, TSEB requires LAI, fractional cover, air temperature (Ta), wind speed, emissivity, radiation parameter, landcover map, geometrical information from the canopy (leaf width, canopy height), and geographical information for the study area (Latitude, Longitude, flight time).

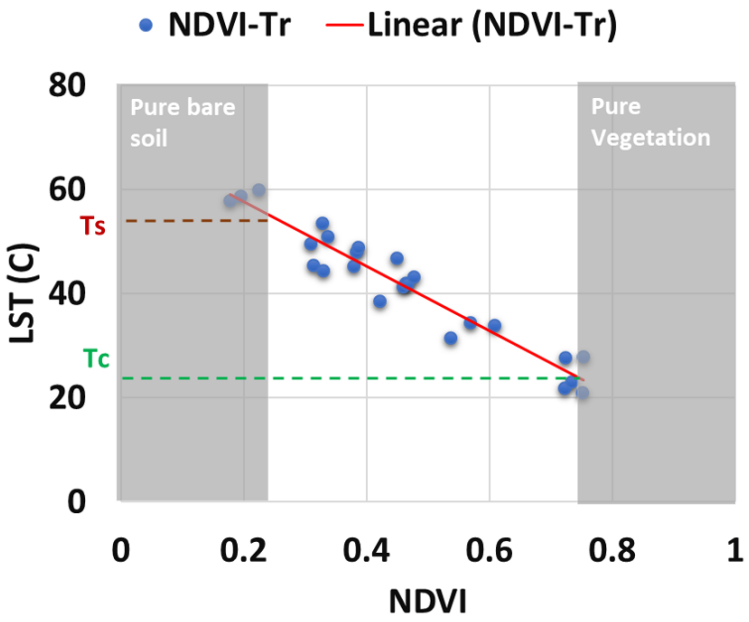

Figure 3. Example of contextual NDVI-Trad scatterplot used for searching Ts and Tc within a 3.6 m grid.

In TSEB models, roughness, net shortwave (Sn) and longwave radiation (Ln) are generally calculated at the first steps. Next, net longwave radiation is separated into canopy and soil net longwave radiation (Ln_s and Ln_c) using the research conducted by Kustas and Norman (1999[21]). Then net radiation at the soil and canopy is calculated based on the summation of net longwave and shortwave radiation for each component (Rn_s and Rn_c). Since it is assumed that the soil heat flux (G) is a portion of Rn_s (e.g. 35%), it is simply calculated in this step. Afterward, sensible heat flux is estimated for the canopy and soil components (H_s and H_c) assuming a stable atmospheric condition, and it is corrected in a loop until it satisfies the stopping criteria (e.g., differences between consecutive Monin-Obukhov length is less than 0.00001). Ultimately, latent heat flux is calculated for soil and canopy (LE_s and LE_c) using Eqs. (4) and (5).

$$LE_S = Rn_S - G - H_S\,, \tag{4}$$

$$LE_C = Rn_C - H_C. \tag{5}$$

2.3 Histogram Analysis

Considering the four shadows scenarios (original, shadow removal, shadow compensation by LCC, and shadow compensation by GC) and applying the described technique to separate Tr into Ts and Tc on three sets of AggieAir UAV imagery, different Ts and Tc distributions for each of the scenarios are achieved. These distributions are shown in Fig 4.

Fig 4 shows the impact of shadows on Tr separation into Ts and Tc. Visually, these histograms display significant differences. In general, applying both shadow removal and compensation techniques provide lower values for Tc compared to the original imagery (the peak of histograms are shifted to the left). However, these shifts can depend on phenological stages and the scenarios. For instance, after applying the GC method, the values of Tc are still similar to Tc from the original imagery. In July 2015, the impact of shadow compensation by LCC and shadow removal is quite apparent. For this date, while the Tc histogram from GC mitigated the Tc from the original imagery, LCC and shadow removal led to cooler canopy temperatures (up to 10 Celsius change in the histogram peaks). In terms of Ts, shadow compensation by LCC provides higher values in comparison with

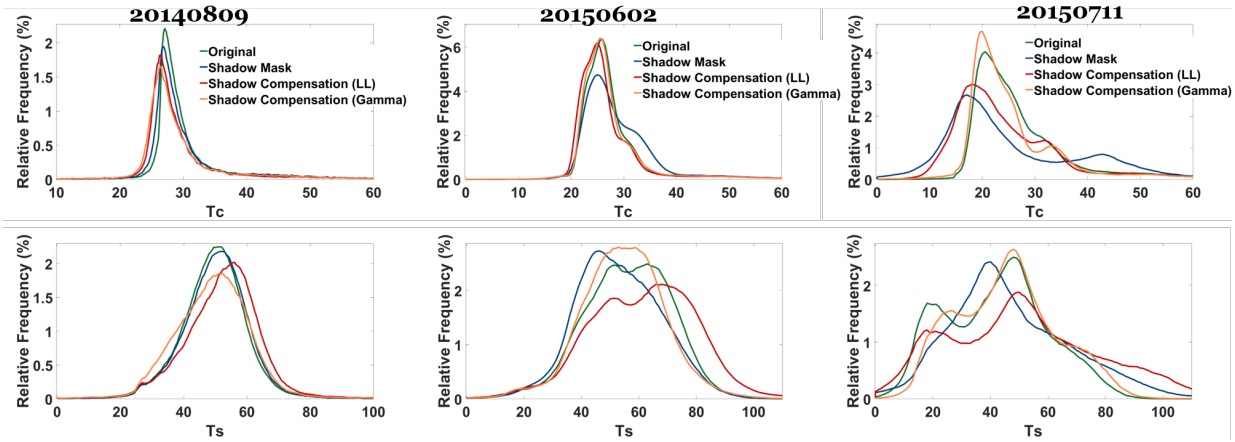

Figure 4. Histograms of Ts and Tc achieved based on four different scenarios.

the original, while employing shadow compensation by GC and shadow removal lead to cooler Ts. In general, it can be concluded that the impact of these scenarios on Ts and Tc from Tr can be significant. However, it would be more important to asses their impact on the performance of ET models versus flux tower records.

2.4 Impact of shadow removal and shadow compensation on TSEB-2T model

To evaluate the impact of shadow scenarios on the performance of ET models, the TSEB-2T model is executed using four different Ts and Tc distributions, and the model results are compared with flux tower measurements (observed values). The other parameters such as LAI and meteorological parameters are kept the same. Fig 5 shows the TSEB-2T model fluxes for four scenarios versus the flux tower records for the 2014 August flight.

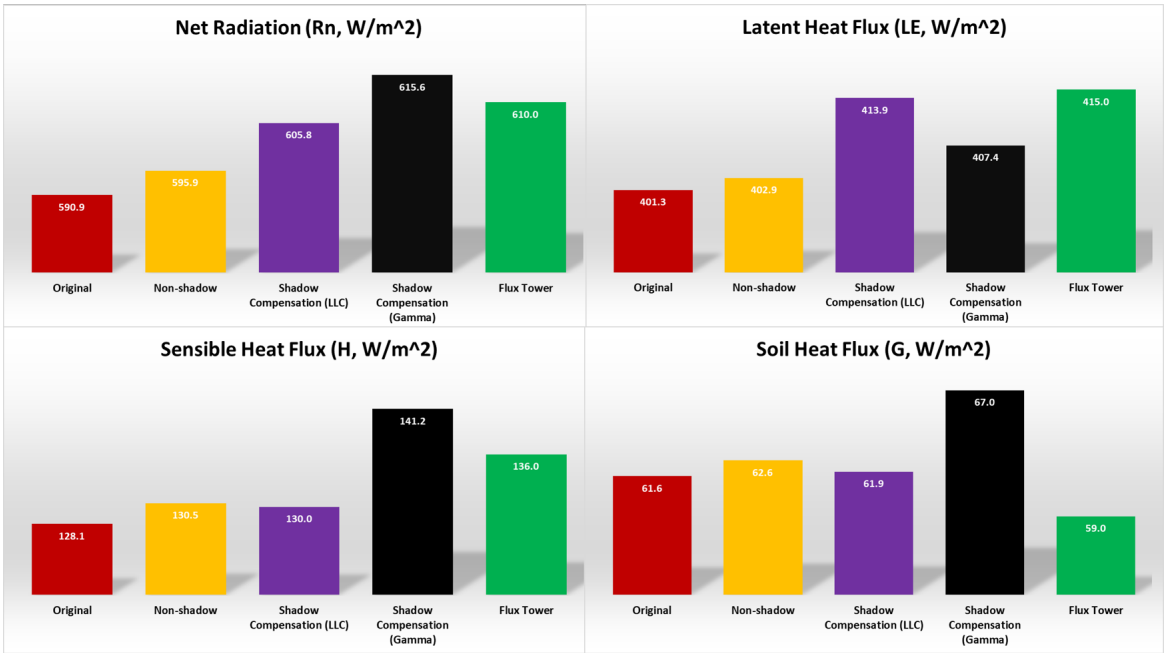

Figure 5. Bar charts showing TSEB fluxes for different scenarios versus flux tower records

As shown in Fig 5, all shadow compensation and shadow removal methods lead to an improvement in Rn, LE, and H fluxes compared to the eddy covariance records, but not in G. Shadow compensation by GC enhanced the performance of the TSEB model, particularly in Rn and H estimates, while the LCC method improved the

LE component in the TSEB model. Therefore, the GC approach outperformed the original, LCC, and shadow removal scenarios in Rn and H estimates, whereas the LCC approach worked better than other scenarios in LE estimates. Concerning G, the original imagery (with no processing for shadows) is the closest to the flux tower measurement. The original, LCC, and shadow removal approach are quite similar to one another in G and H estimates, but the GC approach overestimated both G and H fluxes. Therefore, different scenarios have different impacts on each flux.

Fig 6 illustrates the full comparison between TSEB results and eddy covariance records for three sets of AggieAir UAV imagery.

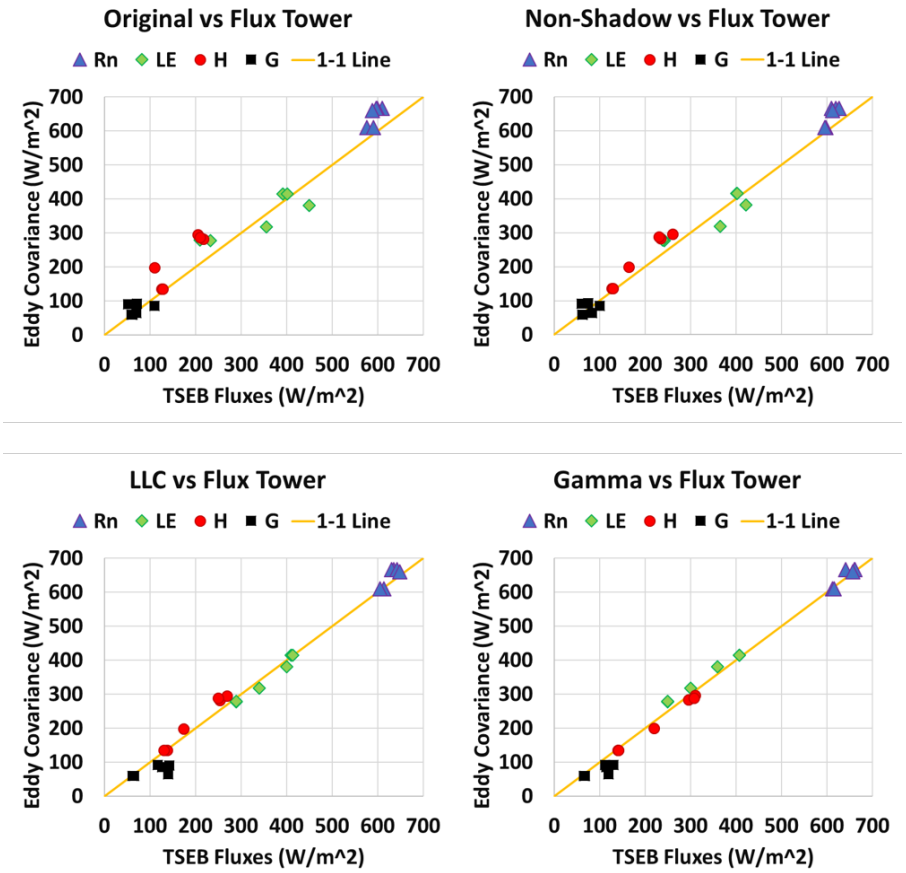

Figure 6. Scatter plots showing TSEB fluxes for different scenarios versus flux tower records

The TSEB model results are extracted in the flux tower footprint regions for each flight, and the comparison between the modeled fluxes and observed record are shown in Fig 6. As illustrated, the agreement between TSEB fluxes and flux tower records is higher after applying shadow removal and shadow compensation methods in comparison with the original. The overestimation of G and H components from the TSEB model in the GC scenario is comparable with the TSEB-2T results for the 2014 flight (bar chart Fig 5). In addition, among shadow compensation and removal methods, the results of TSEB under the shadow removal scenario seem more similar to the original than to the others. The only improvement is for H component, but the other fluxes are quite close to the original. The LCC and GC scenarios show quite similar impacts on G and Rn, but not on H and LE. Their performances on LE and H are in the opposite direction. However, the agreement between LE from the LCC scenario and LE from flux tower is higher than LE from the GC approach.

3. CONCLUSION

Shadows can be a useful source of information or a challenge in aerial imagery. With increasing resolution, shadows become more important. Shadows can have a significant impact on VIs and consequently can affect the performance of energy balance models if they are dependent on VIs. Four different scenarios and three sets of UAV imagery are considered to evaluate the impact of shadows on TSEB-2T models. Results indicated that both removing and compensating for shadows led to lower values for Tc, and compensation led to higher values for Ts, but removal did not. Both shadow compensation methods work better than the shadow removal approach and lead to an improvement in LE and H estimates from the TSEB model. However, shadow compensation by G led to an overestimation in both G and H.

ACKNOWLEDGMENTS

The authors would like to thank Carri Richards for editing the manuscript and the Utah Water Research Laboratory for financially supporting this project.

REFERENCES

[1] Shahtahmassebi, A., Yang, N., Wang, K., Moore, N., and Shen, Z., "Review of shadow detection and de-shadowing methods in remote sensing," Chinese Geographical Science. **23**, 403-420 (2013).

[2] Dare, P. M., "Shadow analysis in high-resolution satellite imagery of urban areas," Photogrammetric Engineering and Remote Sensing. **71**, 169-177 (2005).

[3] Aboutalebi, M., Torres-Rua, A., McKee, M., Kustas, W.P., Nieto, H., and Coopmans, C., "Validation of digital surface models (DSMs) retrieved from unmanned aerial vehicle (UAV) point clouds using geometrical information from shadows," *Proc. SPIE* **11008**, Autonomous Air and Ground Sensing Systems for Agricultural Optimization and Phenotyping III, 1100819 (2019).

[4] Singh, K.K., Pal, K., and Nigam, M.J., "Shadow detection and removal from remote sensing images using NDI and morphological operators," International Journal of Computer Applications. **42**(10), 37–40 (2012).

[5] Tolt, G., Shimoni, M., and Ahlberg, J., "A shadow detection method for remote sensing images using VHR hyperspectral and LiDAR data," In Proceedings of the 2011 IEEE International Geoscience and Remote Sensing Symposium (IGARSS). Vancouver, BC, Canada, 4423-4426 (24-29 July 2011).

[6] Chen, Y., Wen, D., Jing, L., and Shi, P., "Shadow information recovery in urban areas from very high resolution satellite imagery," International Journal of Remote Sensing. **28**(15), 3249–3254 (2007).

[7] Garousi-Nejad, I., Tarboton, D., Aboutalebi, M., and Torres-Rua, A., "Terrain analysis enhancements to the height above nearest drainage flood inundation mapping method," Water Resources Research. In press (2019).

[8] Aboutalebi, M., Torres-Rua, A., Kustas, W.P., Nieto, H., Coopmans, C., and McKee, M., "Assessment of different methods for shadow detection in high-resolution optical imagery and evaluation of shadow impact on calculation of NDVI, and evapotranspiration," Irrigation science. 1–23 (2018). DOI: 10.1007/s00271-018-0613-9.

[9] Sarabandi, P., Yamazaki, F., Matsuoka, M., and Kiremidjian, A., "Shadow detection and radiometric restoration in satellite high resolution images," IGARSS 2004. **6**, 3744–3747, (2004).

[10] Massalabi, A., He, D.C., Bni, G.B., and Beaudry, E, "Detecting information under and from shadow in panchromatic Ikonos images of the city of sherbrooke," IGARSS 2004. **3**, 2000–2003 (2004).

[11] Tsai, V.J.D., "A comparative study on shadow compensation of color aerial images in invariant color models," IEEE Transactions on Geoscience and Remote Sensing. **44**(6), 1661–1671, (2004).

[12] Yamazaki, F., Liu, W., Takasaki, M., "Characteristics of shadow and removal of its effects for remote sensing imagery," Proc. IEEE IGARSS IEEE, IV-426IV-429 (2009).

[13] Aboutalebi, M., Torres-Rua, A., McKee, M., Kustas, W.P., Nieto, H., and Coopmans, C., "Behavior of vegetation/soil indices in shaded and sunlit pixels and evaluation of different shadow compensation methods using UAV high-resolution imagery over vineyards," *Proc. SPIE* **10664**, Autonomous Air and Ground Sensing Systems for Agricultural Optimization and Phenotyping III, 1066407 (2018).

[14] Nieto, H., Kustas, W.P., Torres-Ra, A., Alfieri, J.G., Gao, F., Anderson, M.C., White, W.A., Song, L., del Mar Alsina, M., Prueger, J.H., McKee, M., Elarab, M., and McKee, L.G. "Evaluation of TSEB turbulent fluxes using different methods for the retrieval of soil and canopy component temperatures from UAV thermal and multispectral imagery," Irrigation Science. (2018). https://doi.org/10.1007/s00271-018-0585-9

[15] Kustas, W.P., M.C. Anderson, J.G. Alfieri, K. Knipper, A. Torres-Rua, C.K. Parry, H. Nieto, N. Agam, W.A. White, F. Gao, L. McKee, J.H. Prueger, L.E. Hipps, S. Los, M.M. Alsina, L. Sanchez, B. Sams, N. Dokoozlian, M. McKee, S. Jones, Y. Yang, T.G. Wilson, F. Lei, A. McElrone, J.L. Heitman, A.M. Howard, K. Post, F. Melton, and C. Hain, "The grape remote sensing atmospheric profile and evapotranspiration experiment (GRAPEX)," Bulletin of the American Meteorological Society. **99**, 1791-1812 (2018).

[16] Neale, C.M., and Crowther, B.G. "An airborne multispectral video/radiometer remote sensing system: development and calibration. Remote Sensing of Environment. **49**(3), 187-194 (1994).

[17] Crowther, B.G. "Radiometric calibration of multispectral video imagery." Doctoral dissertation, Utah State University. Department of biological and Irrigation Engineering, (1992).

[18] AgiSoft, L. L. C., and Russia St Petersburg. "Agisoft photoscan," Professional Edition (2016).

[19] Elarab, M., Ticlavilca, A.M., Torres-Rua, A.F., Maslova, I., and McKee, M. "Estimating chlorophyll with thermal and broadband multispectral high resolution imagery from an unmanned aerial system using relevance vector machines for precision agriculture," International Journal of Applied Earth Observation and Geoinformation. **43**, 32–42 (2015).

[20] Torres-Rua, A. "Vicarious calibration of sUAS microbolometer temperature imagery for estimation of radiometric land surface temperature," Sensors. **17**(7), 1449 (2017).

[21] Kustas, WP, Norman, JM, "Evaluation of soil and vegetation heat flux predictions using a simple two-source model with radiometric temperatures for partial canopy cover," Agricultural and Forest Meteorology. **94**(1),13-29 (1999).